OMAE2022-79208

FULL SCALE CFD VALIDATION USING SHIP PERFORMANCE AND WAVE PATTERN MEASUREMENTS OF A MEGA CRUISE SHIP

D.R. Schouten
Maritime Research Institute Netherlands (MARIN)
Wageningen
The Netherlands

A. Drouet
Chantiers de l'Atlantique
Saint-Nazaire, France

M. Birvalski
Maritime Research Institute Netherlands (MARIN)
Wageningen
The Netherlands

L. Morand
Chantiers de l'Atlantique
Saint-Nazaire, France

ABSTRACT

The shipping industry is directly impacted by the global challenge of reducing greenhouse gas emissions. Improvements can be achieved by hull form optimization when designing new ships. Computational Fluid Dynamics (CFD) is nowadays regularly applied for basic resistance simulations as well as for e.g. self-propulsion with rotating propellers or maneuvering in waves. In order to avoid scale-effects, it is increasingly common to perform ship scale CFD calculations. Unfortunately, the available full scale data that can be used for validation are limited. Specifically, flow velocity and radiated wave pattern data are rare at full scale because of the complexity of performing such measurements. Nevertheless, in the current work, full scale wave pattern measurement were performed on a 330 meter long cruise ship sailing at 20 knots using the Digital Image Correlation technique. This is an image analysis method capable of measuring deformations of a surface in space. The approximate size of the field of view was 75 m by 30 m. The ship's speed, shaft power, propeller rate, motions and environmental waves were measured as well. Additionally, Reynolds Averaged Navier-Stokes (RANS) simulations were performed using STARCCM+. The propeller was modelled both as an actuator disk as well as a rotating propeller with a sliding interface. The turbulence closure model was k-ω SST and the free surface was modelled using the Volume of Fluid method. The balance between hull resistance and propeller thrust was verified as a first step, showing less than 4.0% difference. The power determined by CFD was validated against the one measured during the sea trials with less than 3.6% difference. Finally, the comparison of the stern wave pattern resulting from full scale CFD simulations with the pattern measured using DIC showed excellent agreement with good accuracy.

Keywords: Sea trials validation, stern wave measurements, full scale CFD, STARCCM+, Digital Image Correlation, VIC-3D.

1 INTRODUCTION

Chantiers de l'Atlantique asked MARIN to measure stern waves during the sea trial on MSC Cruises Ship to correlate our CFD computations with full scale measurement.

This joint paper presents the way to perform an accurate stern wave measurement by MARIN and a summary of the CFD set up using StarCCM+, which represents results of years of research done by Chantiers de l'Atlantique to determine an appropriate CFD computations set up for speed power prognosis.

The results of the correlation of stern wave measurement between CFD computations performed by Chantiers de l'Atlantique and MARIN's measurement are presented. Furthermore a correlation in terms of speed power is shown.

1.1 CFD numerical process

CFD is being used at Chantiers de l'Atlantique for several years. It is being continuously improved thanks to R&D projects. CFD tools were initially validated and used on bare hull at model scale, while nowadays it is common to see complex full scale simulations including a rotating propeller with a cavitation model. Propulsion simulations could be roughly divided into scenarios involving the propeller model (actuator disk or discretized) and the scale (model and full), resulting in 4 groups. First, propulsion CFD simulations were carried out at model scale with an actuator disk ([1] and [2]). With the increase of CPU resources simulations with a discretized propeller were made possible, but still at model scale by various researchers ([3], [4], [5], [6], [7] and [8]).

Historically, CFD solvers were validated against model scale experiments from towing tank tests. Considering scale effects and extrapolation issues, there are large benefits in performing full scale CFD simulations. Full scale simulations were first computed with an actuator disk model ([9] and [10]) and then with a rotating propeller ([11]), but without comparison to full scale data. The first comparison with sea trials data were presented in [12] and [13], showing promising results, but they were limited to power time series as a function of the speed. Cruise ship sea trials were identified as a good opportunity to collect ship scale data like speed power time series, but also stern wave patterns to be used later for full scale CFD validation. This paper presents the full scale data collection and its comparison with CFD propulsion simulations.

1.2 Digital Image Correlation

Digital Image Correlation technique (DIC) is an image analysis method capable of measuring the displacements and deformations of an object in space. Working with either one or two cameras, two dimensional or three-dimensional measurements can be performed respectively. The 3D measurements are based on the stereoscopic principle [14], in which grey value patterns in the image are cross-correlated. The technique works when the surface of the object has a random speckle pattern with no preferred orientation (isotropic) and with a high contrast. The size of the features in the pattern should be large enough to distinguish them as features. If the surface does not contain a suitable speckle pattern by itself, it must be applied through printing or painting. DIC is an established measurement technique within MARIN [15], [16] and [17].

In the current work, the DIC technique was applied on a very large scale. The height and shape of the stern waves behind a mega cruise ship were measured in three-dimensional space using two cameras. The size of the area of interest was approximately 75 by 30 meters. For the DIC analysis, commercial software from Correlated Solutions was used. All image processing was done with VIC-3D. The post processing was done with in-house tools in MATLAB.

2 SEA TRIALS DATA

The quantities measured onboard were: stern wave height using DIC, ship speed with a D-GPS, ship motions with a motion sensor and environmental wave statistics using a wave buoy. In this paper, the focus is mainly on the stern wave measurements performed with two cameras and analyzed with digital image correlation.

2.1 Ship Data Recording

The ship speed over ground is derived from the ship trajectory issued from D-GPS recorded at 1 Hertz. The delivered power is recorded from the electrical consumption of the POD electrical engine at 1 Hertz.

Environmental conditions are also recorded at 1 Hertz: wind speed and direction, air temperature and pressure are obtained from the anemometer and weathercock temporarily installed for the sea trials. The significant wave height, peak wave period and

main wave direction during the speed runs were measured with a wave buoy (Datawell Directional Waverider DWR-G4), moored in the speed test area. The buoy can distinguish both swell and wind wave. The wave characteristics were issued from wave buoy motion time series for each run with a minimal time period of 30 min. The sea water temperature was given by a sensor located at water intakes of the ship. Considering the slow temperature variations, this variable is not recorded at high frequency, but taken when each run starts. The water current was derived from the sea trials analysis based on British Ship Research Association (BSRA) methodology ([18]). Finally, the speed through water, which is the speed used in the CFD simulations, is computed using the speed over ground and the current.

2.2 Stern Wave measurements

2.2.1   Camera position

To observe the aft waves of the ship, the cameras were placed on deck 14 at about 35 meters above the waterline. The balconies of deck 14 had sufficient overhang to avoid obstructions caused by Deck 8, see figure 1. The first stern wave peak from the transom was expected at 7 meters distance, so the blind spot of 4.7 meters behind the transom was no issue. The measurements were performed on the port side of the stern wave, from mid ship to the port beam of the ship.
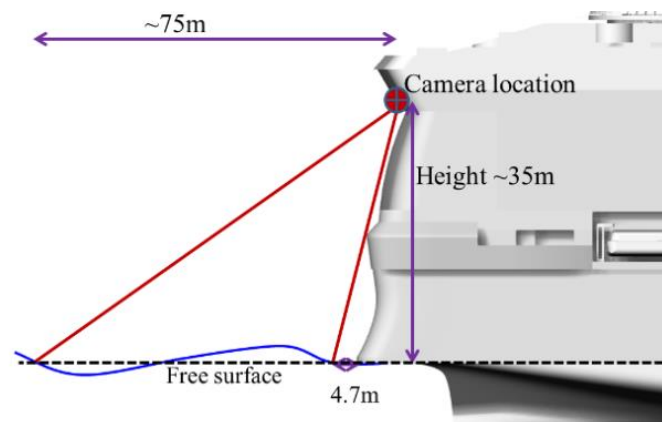

FIGURE 1: Overview of camera location on the aft ship, with height and illustration of camera viewing angle (red lines).

The cameras were installed with passive magnets on two main bulkheads on deck 14, which formed a sturdy foundation, see figure 2 and figure 3.

The distance between the cameras was 8.3 m, placed 1.2 m above deck 14. The two cameras were triggered simultaneously and they had a resolution of 1936x1216 pixels, with 11 mm Kowa zoom lenses attached.

FIGURE 2: One of the cameras on port side bulkhead.

FIGURE 3: Side view of the port side camera. The other camera can be seen in the distance.

2.2.2 Camera calibration and coordinate system

The calibration of the DIC setup resulted in the position and the orientation of the cameras relative to each other, as well as distortion coefficients of the camera lenses. For the current application, the calibration needed to be performed in the following steps:

- Lens calibration, to correct for the lens distortions.
- Disparity calibration, to determine the orientation of the cameras with respect to each other.
- Distance calibration, converts the arbitrary pixel space into SI-unit space.

The VIC-3D software allowed for a separate calibration, which runs through the three calibration steps. The lens calibration was done with a calibration board. The disparity calibration was done by creating an image which contained a speckle pattern in the region of interest. Since this region was the water surface behind the ship, a large speckle screen of 4x4 meters was sailed around with a motorboat. All subsequent images were stitched to create a calibration image, see figure 4 and figure 5.
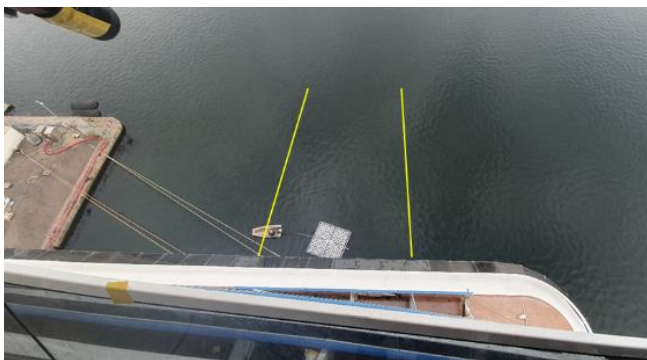

FIGURE 4: Towing of the calibration screen. The yellow lines indicate the centerline and port side beam of the ship determined using a rope tied to the ship and stretched out over the water.
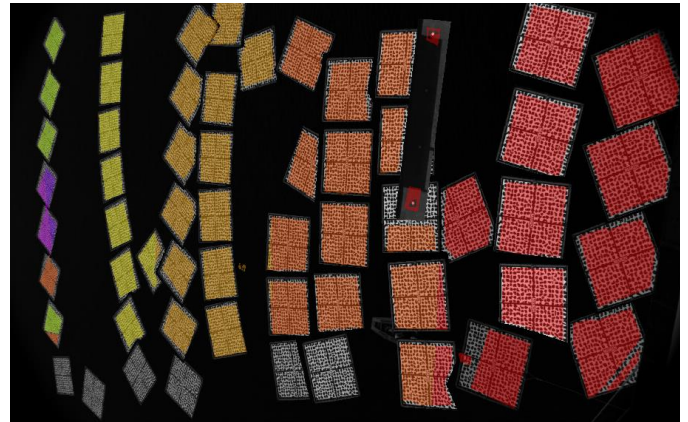

FIGURE 5: Processed composite image of the calibration screen. The cameras are on the right side of the image, i.e. the image is flipped 90 degrees anti-clockwise.

The distance calibration is preferably done using a large object in order to minimize the error. When sailing through a lock, two dots on the lock gates provided a relatively long distance of 9.94m that was used to scale the images, see figure 6.
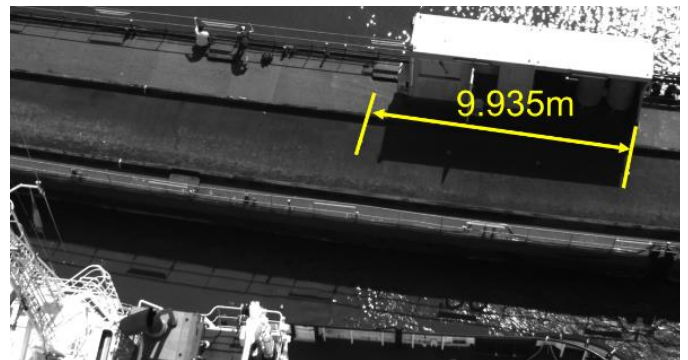

FIGURE 6: Measured distance on a flat lock gate between two round markers 9.94 m apart.

The coordinate system was aligned by placing the calibration screen in line with the ship's centerline and measuring the distance from the transom to the screen, see figure 7, figure 8 and figure 9. Positive X-direction is towards the bow of the ship, positive Y is towards the port side and positive Z is vertically upwards.
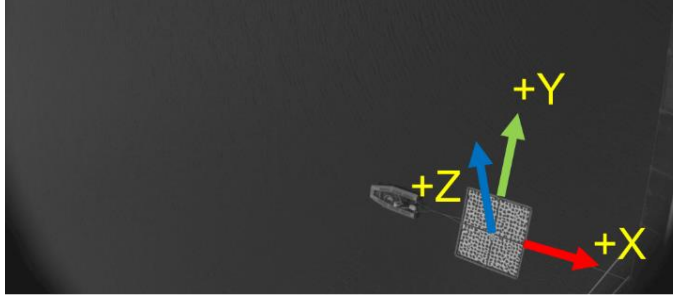
FIGURE 7: Calibration screen aligned with the centerline of the ship. The cameras are on the right side of the image, like in figure 5.
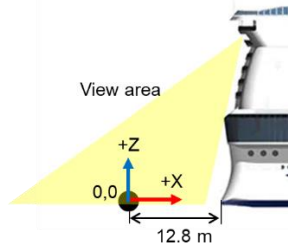

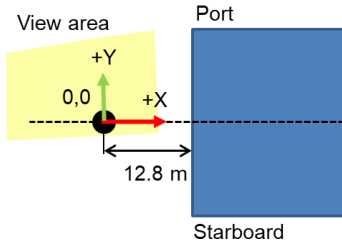
FIGURE 8: Side view of aft ship.

FIGURE 9: Top view of aft ship.

2.2.3   Tests during sea trials

The camera measurements were performed during the sea trials of the ship. Speed runs of 10 minutes length were executed, in which the speed and heading of the ship were kept constant with minimum steering. The speed runs varied between 20 and 22 knots. The images were recorded at 2 Hertz, resulting in two times 1200 images per run. Additionally, tests were performed at zero ship speed to determine the flat water level and orientation. This was necessary as the draught changed after the ship left the port.

2.2.4   Analysis procedure

The general wave shape and height behind the ship can be considered steady with constant ship speed and heading. Therefore, all 1200 images per 10 minute tests were averaged, averaging also the fluctuations naturally present on the water surface. Furthermore, the DIC measurement included the effects of ship motions and immersion of the aft ship with increasing ship speed. Immersion of the ship was difficult to measure accurately on the open sea. Instead, the immersion was calculated from CFD, which was around 25 cm, and the CFD results were corrected accordingly to compare with the DIC data. The ship motions were measured together with the DIC measurements to make corrections possible. However, the ship motions averaged over the speed run duration were found to be negligible during the trials, so no additional corrections were applied.

The processing of the images was done using commercial software (Correlated Solutions, VIC-3D). In batch processing mode, images could be automatically processed. The post processing, including the averaging, translation, rotation and plotting of the data, was done via dedicated MATLAB scripts.

2.2.5   Accuracy of camera setup

In the current measurements, the accuracy of the DIC system depends on:
- Lens calibration uncertainty, approximately 0.07 mm.
- Disparity uncertainty, approximately 4 mm.
- Distance uncertainty, approximately 20 mm.
- Uncertainty of the reference object (flat water surface), approximately 30 mm.

First, the lens calibration was performed by placing a calibration target in front of the lens. The procedure to correct for lens distortion is straightforward and results typically in small errors, in this case around 0.07 mm.

Secondly, the disparity calibration results in a theoretical model describing the camera orientation. The fit of the model results in an error expressed in pixels. After the distance calibration, this pixel error was converted to mm error at the area of interest, see figure 10. Overall, the error in Z-direction is low, with a maximum value of 4 mm.

Thirdly, there is uncertainty in the distance calibration. By reverse processing, the distance on the lock gate that was measured using a ruler was retrieved using DIC. This value differed with a maximum of 20 mm from the measured value.

Lastly, the measurements were corrected with the flat water height. The flat water reference was measured during a 2 minute test at sea, when the ship had zero speed. From these data an average reference height was calculated and a plane fit was made through the data. The residue is shown in figure 11, which indicates the potential noise on the data (assuming that the water surface was perfectly flat). The standard deviation is 30 mm with maximum values up to 80 mm. It is important to note that the deviations are random in character and are sufficiently small for the purpose of the measurements.
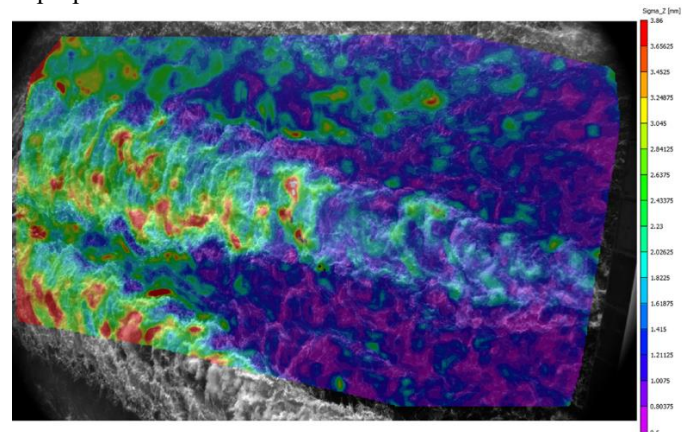

FIGURE 10: Disparity error in Z-direction for a single image, based on the field of view on aft waves. The maximum deviation (red areas) is ~4 mm.
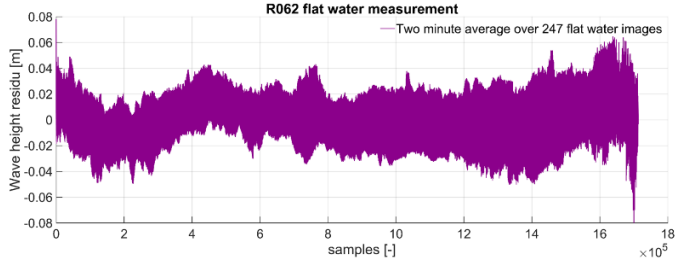
FIGURE 11: Residual water surface after subtracting the averaged surface at zero ship speed during a 2-minute time interval.

3 CFD METHODOLOGY

The wave system behind the ship was calculated with computational fluid dynamics (CFD). The objective is to compare the computations with the sea trial data.

3.1 Geometry and conditions

For the simulations, the ship was fully appended with four bow thruster tunnels equipped with their grids, two fin stabilizer recesses and two pods with propeller and head boxes, see figure 12. The main specifications of the ship are shown in table 1.

FIGURE 12: View of the geometry.

Length between perpendiculars	L_{PP}	m	311.6
Beam	B	m	43.0
Draught	T	m	8.4
Propeller diameter	D_{prop}	m	6.1

TABLE 1: Main dimensions of the ship.

The reference loading condition of the ship was determined in port, prior to departure for the sea trials. The ship's draft was measured together with the water density and all tank levels were recorded. This information referenced the values with the ship's loading system.

The loading condition was determined accurately during speed trials using the loading system which takes into account all the tank levels time series. These loading conditions from the sea trial reports were applied in the computations.

3.2 Computational domains

The ship's computational domain size was chosen to avoid any numerical blockage effect. It is extended 2 L_{PP} upstream, 3 L_{PP} downstream, 1 L_{PP} above, 2 L_{PP} below and 2.5 L_{PP} on the side. Only half of the domain was simulated due to symmetry of the geometry and the expected solution. The computational domain and boundary conditions are illustrated in figure 13. The ship surface refinements, such as bow thrusters, stabilizer recesses and POD thrusters, can be seen in figure 14. Specific refinement boxes were used to capture the wave pattern around the hull, see figure 15. Boundary layers on the ship hull and appendages were adapted to the use of a wall function. About 20 layers were used with a stretching ratio of 1.21 and a total

thickness of 0.1% of L_{PP}. The grid consisted of about 8.6 million trimmed cells.
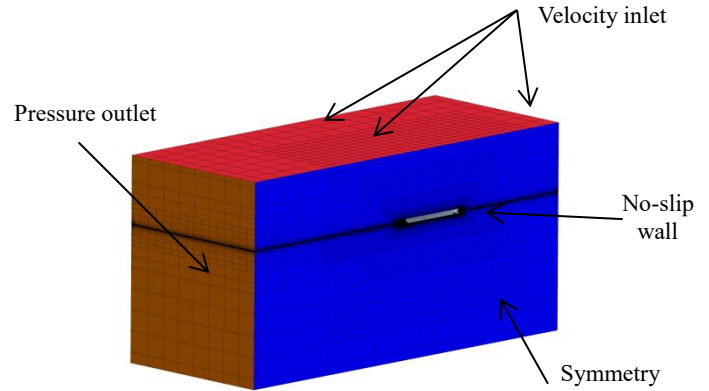

FIGURE 13: Computational domain size and boundary conditions.

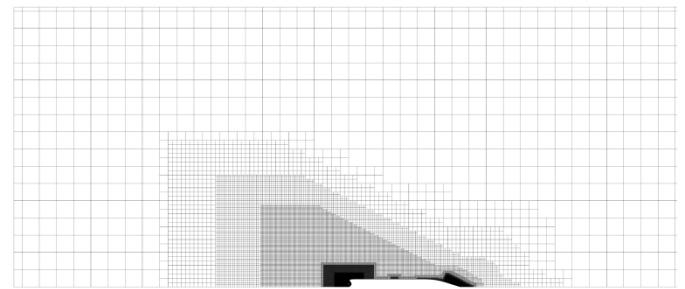**FIGURE 14:** Surface refinements.

FIGURE 15: Free surface refinements.

The rotating propeller simulations used one grid around the ship and one grid around the propeller, which was rotating. The communication between the two grids was done using a sliding interface consisting of a cylindrical surface. The propeller was meshed within a cylinder with a diameter equal to 1.4D_{prop} and a length of 0.6D_{prop}. Boundary layers on the propeller blades were adapted to low Reynolds computation. About 20 layers were used, with a stretching ratio of 1.25 and a total thickness 1.2% of D_{prop}. The propeller grid was made of about 12.9 million polyhedral cells (figure 16). A roughness height of $k_S = 30\ \mu m$ was applied on the propeller blades.

The ship and propeller grids were combined together and used in the rotating propeller simulations. A side view of a Y-slice of the combined grids located at the propeller center is shown in figure 17. The ship's trimmed grid cells are clearly visible together with the propeller grid, which uses polyhedral cells separated by the cylindrical sliding interface.
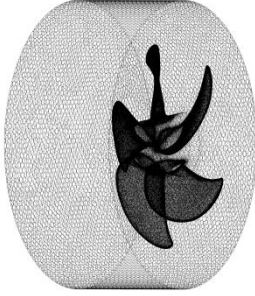
FIGURE 16: Propeller grid with the cylindrical sliding interface.

For rotating propeller simulations, the ship was fixed in its heave and trim position. These were determined based on appended propulsion simulation using a simplified propeller model based on actuator disk theory. A specific grid, with local refinement for the actuator disk was generated for this preliminary simulation (figure 18). Note that the meshed propeller and sliding interface were not included in this preliminary simulation.
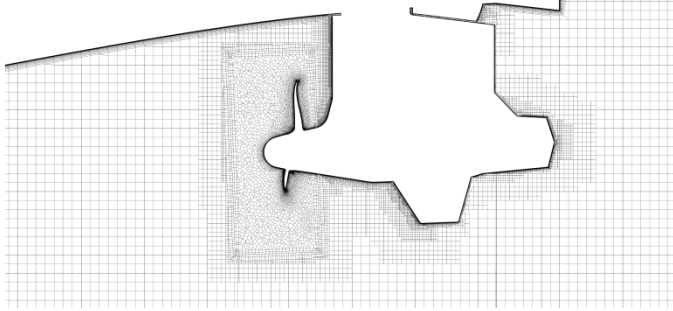

FIGURE 17: Side view of a Y-slice of the propulsion with sliding interface grid – trimmed cells around ship and polyhedral cells around propeller. Bow of the ship is to the left.
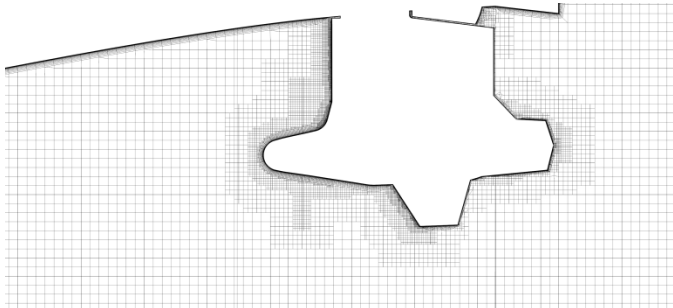

FIGURE 18: Side view of a Y-slice of the propulsion with actuator disk grid – trimmed cells Bow of the ship is to the left.

Modeling approach

All simulations were carried out at full scale using STARCCM+ 2020.2 build 15.04.008. Each speed test was reproduced in CFD taking into account the loading condition, ship speed through water derived from speed over ground and current values, propeller rotation rate and wind speed. Waves were not taken into account, since the sea state was very low during the sea trials. Wind loads, hull roughness and bilge keels

were not considered in the CFD simulation and have to be added in the post processing.

Wind load coefficients were taken from specific aerodynamic CFD simulations taking into account all superstructures:

$$R_{wind} = 0.5\rho_{air}A_x V_{AWS}^2 C_{x_0}$$

with

ρ_{air} $[kg/m^3]$ air density,
A_x $[m^2]$ frontal area,
V_{AWS} $[m/s]$ Relative wind speed,
C_{x_0} $[-]$ wind coefficient based on CFD computations.

Contrary to propeller roughness, which is nearly homogeneous and computed by the turbulence model, hull roughness is heterogeneous, since it comes mainly from weld bead between steel sheets. Roughness allowance is defined by the Townsin equation:

$$\Delta C_f = 0.044\left[\left(\frac{k_s}{L_{WL}}\right)^{\frac{1}{3}} - 10Re^{-\frac{1}{3}}\right] + 0.000125$$

with

k_s $[m]$ roughness of hull surface, for hull $k_S = 125\mu m$,
L_{WL} $[m]$ ship length at water line,
Re $[-]$ Reynolds number.
Then, additional hull roughness drag is given by:

$$R_{roughness} = 0.5\rho_{water}S_{wetted}V_S^2\Delta C_f$$

with

ρ_{water} $[kg/m^3]$ water density,
S_{wetted} $[m^2]$ wetted surface area (from CFD simulation),
V_S $[m/s]$ ship speed,
ΔC_f $[-]$ roughness allowance.

The bilge keels were not included in the simulations. Bilge keels are designed to follow the streamlines, so their resistance is mainly coming from shear forces. The additional drag due to bilge keels is given by:

$$R_{BK} = 0.5\rho_{water}S_{BK}V_S^2\left(C_{f_0} + \Delta C_f\right)$$

with

ρ_{water} $[kg/m^3]$ water density,
S_{BK} $[m^2]$ bilge keels area,
V_S $[m/s]$ ship speed,
C_{f_0} $[-]$ frictional resistance coefficient from ITTC57,

$$C_{f_0} = \frac{0.075}{(\log_{10}(Re) - 2)^2}$$

ΔC_f $[-]$ Roughness allowance.

Propeller open-water simulations were carried out in order to determine the open-water characteristics (K_{T_0}, K_{Q_0} and η_0) that are used by the actuator disk model. The propulsion with actuator disk simulation was carried out for each loading condition with two degrees of freedom, i.e. heave and trim.

The time averaged behavior from the propulsion with actuator disk simulation was then imposed to the ship before generating the mesh of the propulsion with rotating propeller

simulation. This propulsion simulation was carried out with no degree of freedom, apart from the propeller rotation. The propulsion with rotating propeller simulation was carried out in three steps:

1. An initialization phase, about 400 s, where the propeller is not rotating but the flow in the propeller domain is solved thanks to a moving reference frame (MRF) rotating with the propeller rate taken from the time averaged propeller rate from the actuator disk simulation. The time step used for this initialization was similar to the one of the propulsion with actuator disk simulation i.e. $L_{PP}/(200V_S)$

2. Based on this initialization, the computation was restarted replacing the MRF by the propeller rotation through Rigid Body Motion (RBM). During 1.5 s, equivalent to about three propeller rotations, the time step was decreased to a value corresponding to 2° of propeller rotation.

3. About 7 propeller rotations (35 blade passages) were necessary to reach the steady-state regime.

The figure 19 illustrates this methodology showing the thrust coefficient of each propeller blade as a function of the propeller rotation. Negative propeller rotation corresponds to the MRF phase.
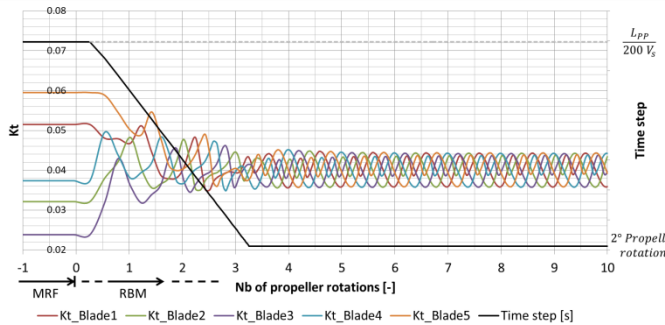

FIGURE 19: Thrust coefficient of each propeller blade as a function of the propeller rotation and time step.

The computational time was respectively about 6 hours on 224 cores and 24 hours on 448 cores for actuator disk and rotating propeller simulations.

4 RESULTS

4.1 Resistance/Thrust balance

It is important to first validate if the self-propulsion point was reached, before comparing the propulsion power and stern waves. The balance between resistance forces integrated over the hull and the appendages and the POD thrusts should be close to zero. In the post processing, resistance corrections from wind loads, bilge keels and hull roughness were added to the hull and appendages resistance. For each speed run, the difference between the thrust of the two POD thrusters and the ship resistance is shown (table 2). Two runs at 87% power and one run at 100% power are presented.

	ST-1_87%	ST-2_87%	ST-4_100%
Diff [% Total Resistance]	-4.0%	-2.9%	-2.3%

TABLE 2: Resistance/Thrust balance from rotating propeller.

The balance between resistance and thrust is below 4% of the total resistance showing that the self-propulsion point is almost reached. The ship resistance and POD thrust are linked to the current velocity. The propeller rate is imposed as well as the ship speed which is determined based the speed over ground measured with D-GPS corrected by the current value. The current is not measured during the sea trials. It is determined from speed runs post-processing based on BSRA methodology. Considering a current coming from the bow, increasing its velocity will contribute to increase the resistance and to decrease the propeller thrust deteriorating the resistance thrust balance at the same time.

A comparison between simulations with rotating propeller and actuator disk is presented in table 3.

	ST-1_87%	ST-2_87%	ST-4_100%
Diff [% Total Resistance]	12.2%	8.3%	9.1%

TABLE 3: Resistance/Thrust balance from actuator disk.

The self-propulsion point is clearly not reached with the actuator disk model, resulting in an average difference of 10%. Table 4 shows the differences in terms of resistance and thrust between simulations with rotating propeller and actuator disk.

	Diff Resistance AD vs SI [% /SI]	Diff Thrust AD vs SI [% /SI]
ST-1_R-87%	1.9%	19.1%
ST-2_F-87%	1.6%	13.3%
ST-4_R-100%	0.6%	12.4%

TABLE 4: Differences in terms of resistance and thrust between rotating propeller and actuator disk simulations.

The resistance, including the thrust deduction is in good agreement between the CFD simulations, varying between 0.6% and 1.9%. Large differences were found on the POD thrust, varying between 12.3% and 19.1%. These differences relate to the errors made on the wake estimation using the actuator disk. It was concluded that the actuator disk model is not good enough to predict the resistance/ thrust balance.

4.2 Power

Secondly, with the self-propulsion point checked, the power estimated by CFD could be compared to the one measured during the sea trials. The CFD power was calculated by multiplying the torque on the propeller (blades + hub) and the rotation rate of the shaft. The power difference between CFD and the sea trials is shown in table 5. Two runs at 87% and one run at 100% power are included.

	ST-1_87%	ST-2_87%	ST-4_100%
Diff [% Measured Power]	-3.6%	-1.6%	-0.5%

TABLE 5: Power estimated by CFD vs onboard measurements.

The power was underestimated from 0.5% to 3.6 % which is considered as excellent results, taking into account the following:

- Difficulties of CFD computation in self-propulsion configuration
- Accuracy of sea trial results including current, waves and aerodynamic corrections
- The use of empirical formula to complete the speed power prognosis with the hull roughness, bilge keels and aerodynamic resistance.

Such level of accuracy is very close to model tests ones. The undervaluation is also related to the overestimation of the current velocity since it contributes to decrease the torque as well as the thrust.

4.3 Wave height from computations

Before comparing computations with the sea trial measurements, the numerical model itself was studied. This included: the propeller modeling, scaling and effects of the propeller wash. These three parameters are discussed below.

First, the stern wave pattern with a rotating propeller was compared with the actuator disk simulation (figure 20). The results were time averaged over one propeller rotation. The figures shows a symmetrical top view on the stern wave, with the top half assigned to the rotating propeller and the bottom part to the actuator disk. The use of actuator disk seems to be capable to predict the stern wave pattern, which differs from the conclusion of the resistance thrust balance and power estimation where the actuator disk model was not accurate enough.
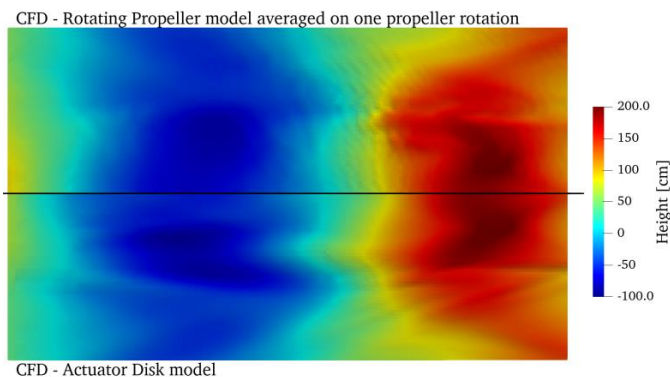

FIGURE 20: Effect of the propeller model on the stern wave pattern. Top part is rotating propeller, bottom part is actuator disk model.

Secondly, a comparison of the stern wave pattern computed at full scale with model scale ($\lambda = 26$) was made (figure 21). The scale effects due to Reynolds differences are clearly visible, showing a rather different stern wave pattern.
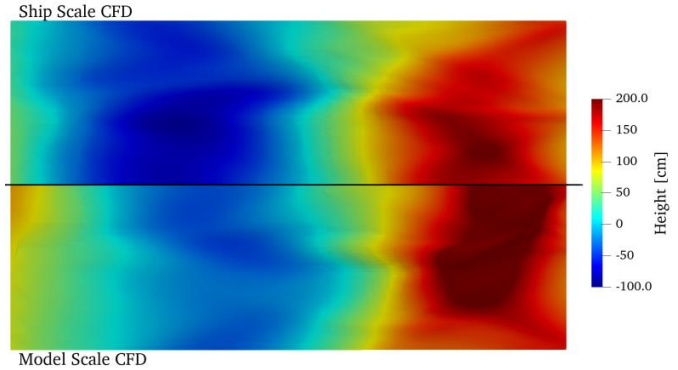

FIGURE 21: Scale effects on the stern wave pattern. Top part is full scale CFD, bottom part is model scale CFD.

Thirdly, actuator disk simulation with propeller effects was compared to a towing resistance simulation (figure 22). The effects of the propeller wash is clearly visible and generates a larger wave top and through behind the ship.
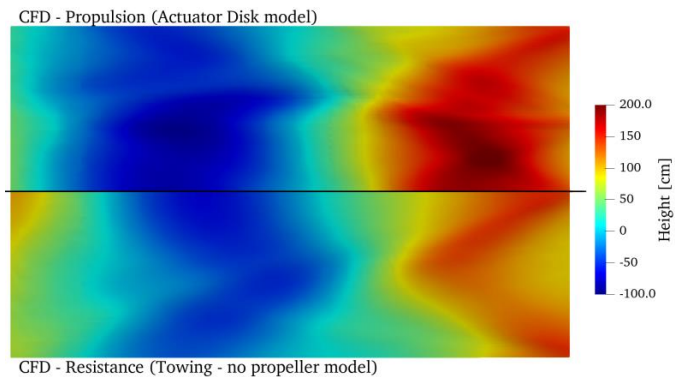

FIGURE 22: Effects of the propeller wash on the stern wave pattern. Top part is with actuator disk, bottom part is a towing simulation.

It is concluded that the scale and the propeller model have a large effect on the stern wave pattern. It is recommended to use full scale CFD simulations and take into account the propeller effects, especially when investigating the stern waves of the ship. Furthermore, this approach improves full scale power prediction and ship stern optimization.

4.4 Wave height from onboard measurements

A view from the mooring deck on the port side part of the stern wave of the ship is shown in figure 23. Looking aft from the transom, the traverse Kelvin waves are clearly visible. The first wave peak (orange line) was observed, followed by a wave trough and a second wave peak (green line). These lines are indicated on the centerline of the ship, in between the starboard and port side propeller wash. The port side edge of the stern wave is indicated with the yellow line. From the side of the ship, a V-shape edge is also present on the stern wave, indicated with the red line.

The waves obtained from the DIC measurements are shown in figure 24 and figure 25. All the details of the wave indicated in the photo are also captured by the DIC. It was possible to

measure the wave height in all the parts of the wave including the area with much foam as well as at the sides.

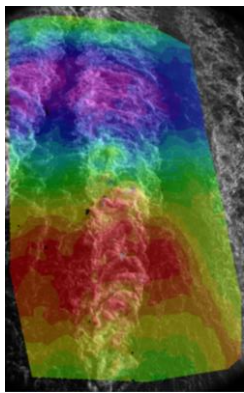**FIGURE 23:** Ship stern wave captured from the mooring deck. Wave shape is indicated with colored lines.

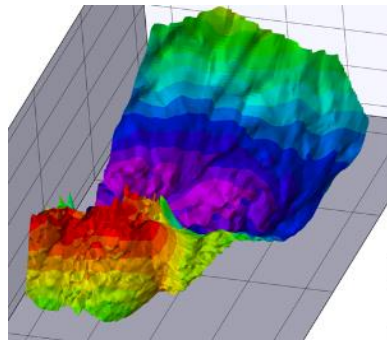**FIGURE 24:** Top view from DIC camera, with data overlay.

FIGURE 25: Instantaneous measured wave shape in 3D.

The ship conditions during one of the speed tests, including heading, speed and pitch motions are shown in figure 26. Note that the pitch motions are very low during the run, though the lever arm for pitch motions is large. By taking images of the stern wave each half second during a 10-minute period, these pitch motions were averaged for the final results.
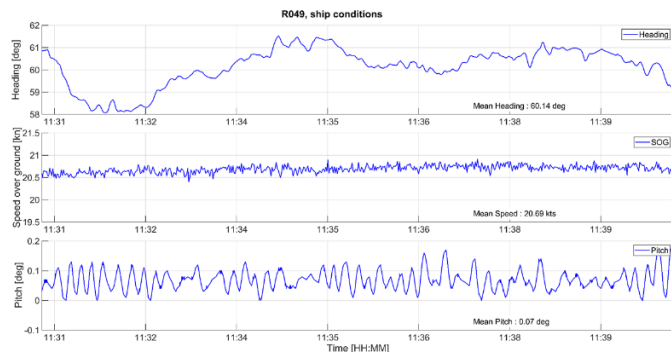

FIGURE 26: Ship heading, speed and pitch motions during run R049-ST-2_F-87%.

5   DISCUSSION

Before comparing the stern wave pattern of the CFD computations with DIC sea trial measurements, both data should be reference to the same plane in space. For the DIC data, the cameras are fixed in the ship reference frame, which includes the ship sinkage and loading conditions. For the comparison, the free surface computed by CFD was aligned with the DIC reference frame, applying the loading conditions, dynamic trim and sinkage from the simulation as an offset value to the surface elevation. The calculated offset value was 25 cm.

First, an overview of the measured area behind the ship is provided (figure 27). The top part of the figure shows an image of the stern wave captured by DIC. The wash of the port side propeller is clearly visible. In the lower left corner of the image, some wash of the starboard propeller is visible. The view area is more than half the width of the ship (21.5 m) and extends from 5 to 75 m aft of the transom of the ship. The bottom part of the figure shows the surface plot of the wave which corresponds with the image area. This surface plot is available from both CFD and from the DIC and will be compared in the following figures.
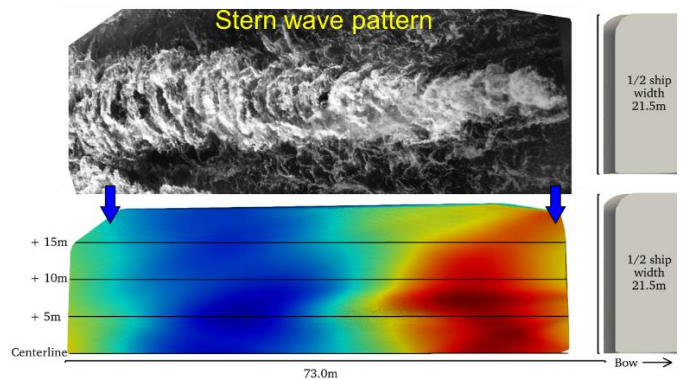

FIGURE 27: Wave cut locations, ship location and main dimensions of the area of interest.

The stern wave patterns from CFD and DIC were compared for three speed runs: two runs at 87% and one run at 100% power. The surface data, cross section data and the differences on the stern wave were compared.

First, the comparisons for run 1 at 87% power are shown in figure 28, figure 29 and figure 30. The stern wave compares well between the measurements and CFD in terms of shape and height. However, some differences occur in the middle of the wash of the propeller (dark red area) and on the left part of the image, where the second stern wave starts to develop.
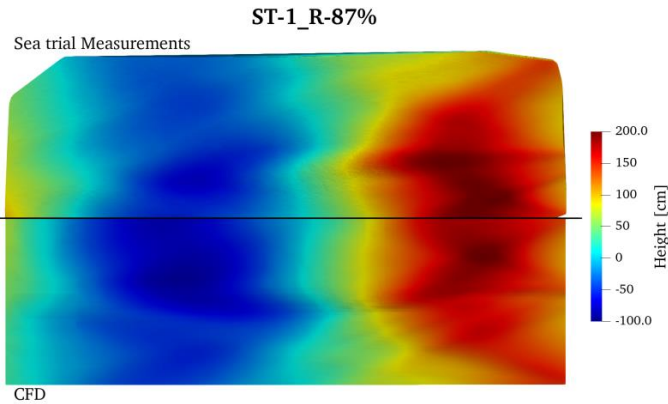
FIGURE 28: Stern wave pattern comparison – CFD (bottom) vs DIC measurements (top) – ST-1_R-87%.

Next, the measured and computed longitudinal cross sections of the wake are compared at the centerline and 15 meters to port from the centerline (figure 29).

From the aft ship (right to left in the figure), it is observed that:

- The measured wave shape correlates well in general with CFD.
- The height of the first wave peak is slightly lower in the CFD at centerline. The difference at this location is mainly due to uncertainties in the simulation of the propeller wash.
- More outward, at 15 meters, the CFD resulted in a wider first wave peak that is slightly higher than the measured one.
- The first wave trough is predicted to be lower by CFD in both cross sections, compared to the measurements.

At the upcoming part of the 2nd wave peak, the CFD predicts a less steep wave.
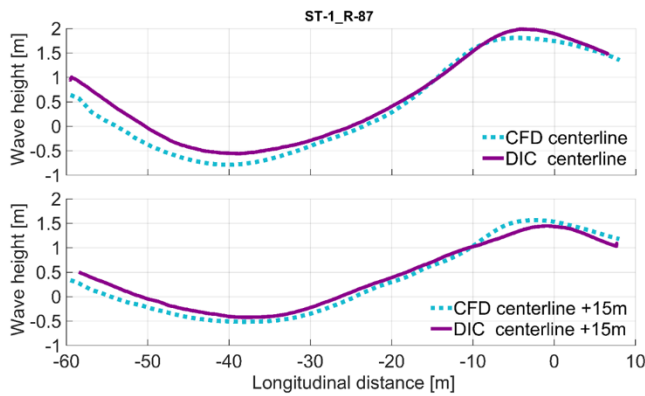

FIGURE 29: Wave cross section – CFD (dashed) vs DIC measurements (solid) – ST-1_R-87%.

Finally, the measured and calculated wave surfaces were subtracted from each other to highlight the differences (figure 30). The values show:

- A mean absolute error of 16.0 cm, which is around 7.9% of the total wave height.
- A surface median of -11.1 cm (5.5%). The lower median indicates mean is influenced by the outliers mainly in the

wash of the propeller. The most common error is smaller, as the median indicates.

Both mean and median values show a sufficiently small difference, 5.5 to 7.9%, between the CFD and measured data.
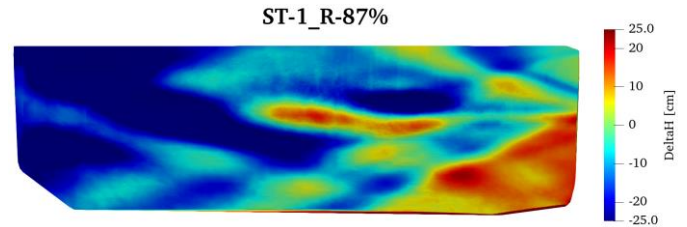

FIGURE 30: Difference between stern waves computed by CFD and obtained from DIC measurements – ST-1_R-87%.

The surface, cross section and differences for run 2, also at 87% power are shown in figure 31, figure 32 and figure 33. The stern wave is a bit lower in this case and the symmetry looks even better (figure 31). Still, differences occur in the wash of the propeller.
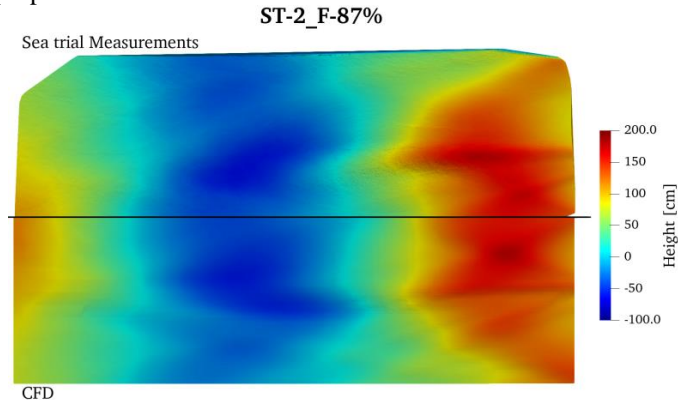

FIGURE 31: Stern wave pattern comparison – CFD (bottom) vs DIC measurements (top) – ST-2_F-87%.
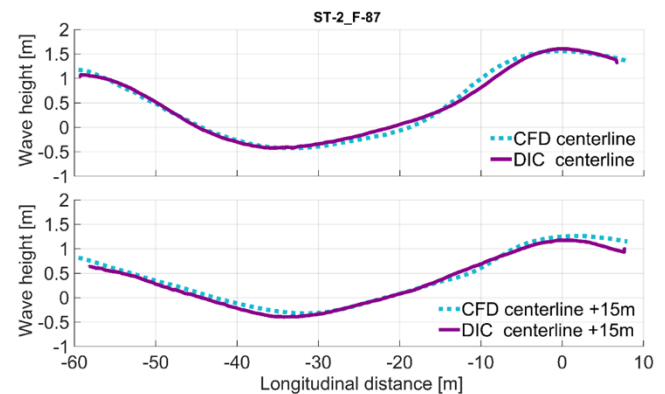

FIGURE 32: Wave cross section comparison – CFD (dashed) vs DIC measurements (solid) – ST-2_F-87%.

From the cross sections (figure 32) it is observed:

- The CFD wave matches well with measurements along the cross section curves.

- The height of the first wave peak and wave trough line up well between CFD and the measurements.
- The CFD results from run 2 match better with the measurements than for run 1.
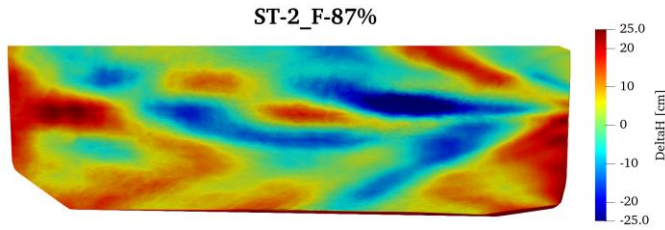
ST-2_F-87%

FIGURE 33: Difference between stern waves computed by CFD and obtained from DIC measurements – ST-2_F-87%.

Also, the difference between the surfaces shows a closer match:
- A mean absolute error for run 2 is 9.8 cm, which is around 5.9% of the total wave height.
- A surface median of 3.1 cm (1.9%).

In run 2, the differences are more equally distributed over the surface area. In run 1, maximum errors are clearly located around the propeller wash. These discrepancies can be correlated to the thrust/ resistance balance, which is lower for run 2 than for run 1, leading to a smaller wave peak.

Run 4 (figure 34, figure 35 and figure 36), at 100% power, shows similar observations as for run 2. Both surface and cross sections correlate well.
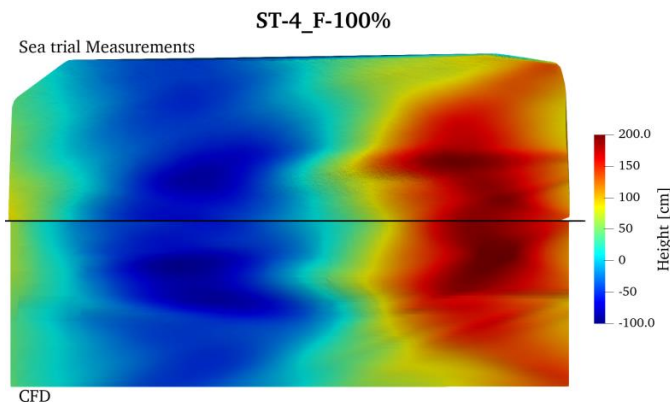
ST-4_F-100%

FIGURE 34: Stern wave pattern comparison – CFD (bottom) vs DIC measurements (top) – ST-4_R-100%.
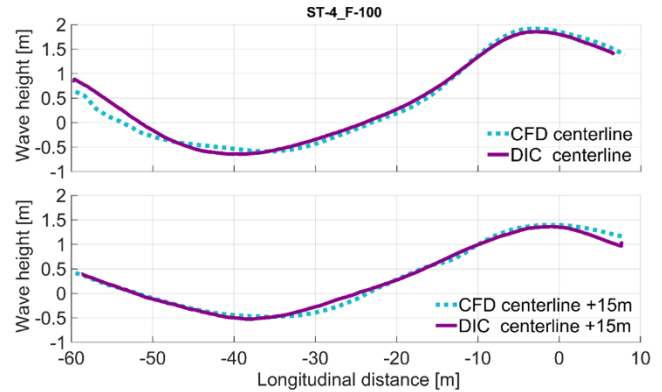

FIGURE 35: Wave cross section – CFD (dashed) vs DIC measurements (solid) – ST-4_R-87%.
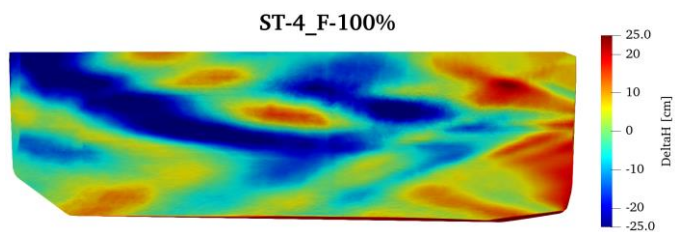
ST-4_F-100%

FIGURE 36: Difference between stern waves computed by CFD and obtained from DIC measurements – ST-4_R-100%.

The difference between the surfaces shows:
- A mean absolute error of 10.4 cm, which is around 5.4% of the total wave height.
- A surface median of -1.7 cm (0.9%).

To conclude, the CFD and the measurements correlate well in the three speed runs. The differences are sufficiently small, in the order of 5% to 8% absolute error of the mean. The median error is lower, ranging from 1% to 5%.

6 CONCLUSION

The DIC technique is able to accurately measure the stern wave of a large vessel at sea. An excellent agreement was obtained between the stern waves patterns resulting from full scale CFD simulations with the patterns measured using DIC. An excellent correlation was also obtained between ship scale CFD and sea trial data in terms of resistance/thrust balance and power. This validation provides confidence in the use of full scale CFD for power prediction, which have the same level of accuracy as model tests results, with limited scale effects and extrapolation issues. The results also show the importance of optimizing the stern hull form in full scale and account for the action of the propellers.

REFERENCES

[1] Pacuraru F., Lungu A., Marcu O. *Self-Propulsion Simulation of a Tanker Hull*, AIP Conf. Proc. 1389, 191, Halkidiki, Greece, 2011

[2] Turnock S.R., Phillips A.B., Furlong M. *URANS simulations of static drift and dynamic manoeuvres of the KVLCC2 TANKER*, SIMMAN 2008: workshop on verification and validation of ship manoeuvring Simulation Methods, Lyngby, Denmark, 2008

[3] Bugalski T., Hoffmann P. *Numerical Simulation of the Self-Propulsion Model Tests*, Second International Symposium on Marine Propulsors SMP'11, Hamburg, Germany, 2011

[4] Carrica P. M., Fu H., Stern F. *Computations of self-propulsion free to sink and trim and of motions in head waves of the KRISO Container Ship (KCS) model*, Applied Ocean Research, Volume 33, Issue 4, 309-320, 2011

[5] Dhinesh G., Murali K., Anantha V. *Estimation of hull-propeller interaction of a self-propelling model hull using a RANSE solver*, Ships and Offshore Structures, Volume 5, Issue 2, 2010

[6] Krasilnikov V. I. *Self-Propulsion RANS Computations with a Single-Screw Container Ship*, Third International Symposium on Marine Propulsors, SMP'13, Launceston, Tasmania, Australia, 2013

[7] Shen H. L., Abdelhak G., Chen Q. T., Su Y. M. *The hydrodynamic performance prediction of ship hull with propeller*, Applied Mechanics and Materials 2012 (Volumes 117 - 119), 598 – 601, 2012

[8] Lin T. Y., Wang Y. S., Wang P. W. , Kouh J. S. *Numerical Simulation of Self-Propulsion Model Tests for a Container Ship*, The 6th Asia-Pacific Workshop on Marine Hydrodymics –APHydro, 2012

[9] Tzabiras G. D. *Self-propulsion simulation of a Series-60, CB=0.6 Hull*, International Multi-Conference on Maritime Research and Technology, Crete, 1-4, 2001

[10] Tzabiras G. D., Polyzos S. P., Zarafonitis G.N. *Self-Propulsion Simulation of Passenger-Ferry Ships with Bow and Stern Propulsors*, 12th Numerical Towing Tank Symposium, Cortona, Italy, 2009

[11] Castro A. M., Carrica P. M., Stern F. *Full scale Self-propulsion computations using discretized propeller for the KRISO container ship KCS*, Computers & Fluids, Volume 51, Issue 1, 15, 35-47, 2011

[12] Ponkratov D., Zegos C. *Ship Scale CFD Self-Propulsion Simulation and Its Direct Comparison with Sea Trials Results*, International Conference on Computational and Experimental Marine Hydrodynamics MARHY'14, Chennai, India, 2014

[13] Ponkratov D., Zegos C. *Validation of Ship Scale CFD Self-Propulsion Simulation by the Direct Comparison with Sea Trials Results*, Fourth International Symposium on Marine Propulsors, SMP'15, Austin, Texas, USA, 2015

[14] Sutton M.A., Orteu J.J., Schreier H. *Image Correlation for Shape, Motion and Deformation Measurements*, Hardcover ISBN 978-0-387- 78746-6, Springer Science + Business Media, 2009

[15] Bunt van de, E., Lafeber, W. *Optical Measurement Techniques in Model Testing*, Advanced Model Measurement Technology, Newcastle upon Tyne, United Kingdom, 2011

[16] Grasso N., Hallmann R., Scholcz T.P., Zondervan G.J.D., Maljaars P., Schouten D.R. *Experimental investigations of the hydro-elastic behaviour of flexible composite propellers in non-uniform flow at model and full scale*, Sixth International Symposium on Marine Propulsors, Rome, Italy, 2019

[17] Sterenborg, J., Grasso, N., Schouten, D.R., & Tjallema, A. *The Ocean Cleanup System* 001 Mechanics and Arctic Engineering (Vol. 58769, p. V001T01A063), American Society of Mechanical Engineers. Performance During Towing and Seakeeping Tests. In International Conference on Offshore, 2019

[18] *BSRA standard method of Speed Trial Analysis*, BSRA Report NS 466, 1978.